ACS Energy LETTERS

http://pubs.acs.org/journal/aelccp

A Si-Substituted Spirobifluorene Hole-Transporting Material for Perovskite Solar Cells

Yanqi Luo,[⊥] Ramesh Kumar Chitumalla,[⊥] So-Yeon Ham, Deniz N. Cakan, Taewoo Kim, Sanghyun Paek, Ying Shirley Meng, Joonkyung Jang,* David P. Fenning,* and Min-cheol Kim*

Cite This: *ACS Energy Lett.* 2023, 8, 5003−5011

Read Online

ACCESS | Metrics & More | Article Recommendations | Supporting Information

ABSTRACT: Hybrid organic−inorganic perovskite solar cells (PSCs) have shown promise for next-generation photovoltaics. This study presents a simple approach for enhancing the performance and stability of PSCs by substituting the center carbon atom of the common hole transport material (HTM) Spiro-MeOTAD with a silicon atom. This modification, termed Si-Spiro, results in an increased hole mobility. A density functional theory simulation indicates that the enhanced hole mobility is due to the structural change of Si-Spiro. Electron beam-induced current microscopy measurements indicate improved charged extraction at the Si-Spiro/perovskite interface. A power conversion efficiency of 22.5% is achieved in Si-Spiro-based PSCs, outperforming standard Spiro-MeOTAD. Additionally, Si-Spiro-based PSCs demonstrate enhanced stability, maintaining over 90% of performance over 120 h of one-sun operation. Depth-profiling X-ray photoelectron spectroscopy revealed that Si-Spiro effectively blocks metal ion migration, which contributes to its enhanced stability. The findings suggest that Si-Spiro could be promising a HTM for high-performing, stable PSCs.

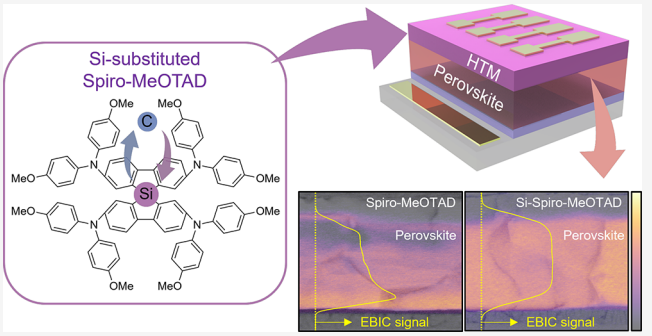

Since their inception in 2009, hybrid organic−inorganic perovskite solar cells (PSCs) have emerged as a promising platform for next-generation photovoltaics, owing to their exceptional efficiency, low production cost, and high chemical/structural flexibility.[1−3] Over the past decade, PSCs have experienced a significant surge in performance, with power conversion efficiencies (PCEs) exceeding 26%.[4−7] However, the rapid development of perovskite solar cells faces significant challenges, primarily the limited progress in achieving long-term device stability when compared to PCE.[8] The instability origins in PSCs can be attributed to various factors, including the intrinsic degradation of the electron transport materials (ETMs) or hole transport materials (HTMs) that make up the PSC,[9,10] as well as the intrinsic degradation of the perovskite absorber layer itself.[11,12] Furthermore, interactions with adjacent layers can lead to mutual influences and contribute to degradation.[13−15] The highest-performing PSCs typically employ a specific device architecture known as the n-i-p configuration,[16] which consists of layers arranged in the following order from the bottom electrode: ETM (n), perovskite absorbing layer (i), HTM (p), and counter electrodes. In high-performing n-i-p devices, the use of polymers or small-molecule-based organic materials for HTMs has been a major concern due to their frequent inherent instability. For example, organic HTMs such as 2,2′,7,7′-tetrakis(*N*,*N*-di-*p*-methoxyphenyl)-amine-9,9′-spirobifluorene (Spiro-MeOTAD) or poly(triarylamine) (PTAA) are commonly used.[9] Their inferior stability is primarily due to the intrinsic vulnerability of such HTMs, the necessary additives for improved hole mobility, and metal ion migration from the top electrode penetrating through the HTMs.[17−19]

While numerous attempts have been made to investigate alternative HTMs that have better performance and stability, no candidate has yet surpassed the efficiency performance of Spiro-MeOTAD.[20,21] Spiro-MeOTAD has a spirobifluorene backbone, where two fluorene units (three-ring structures) are connected at a single carbon with methoxy triarylamine side groups attached to its benzene rings. Many attempts to modify

Received: September 18, 2023
Revised: October 16, 2023
Accepted: October 20, 2023
Published: November 6, 2023

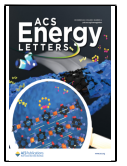

https://doi.org/10.1021/acsenergylett.3c01964
ACS Energy Lett. 2023, 8, 5003−5011

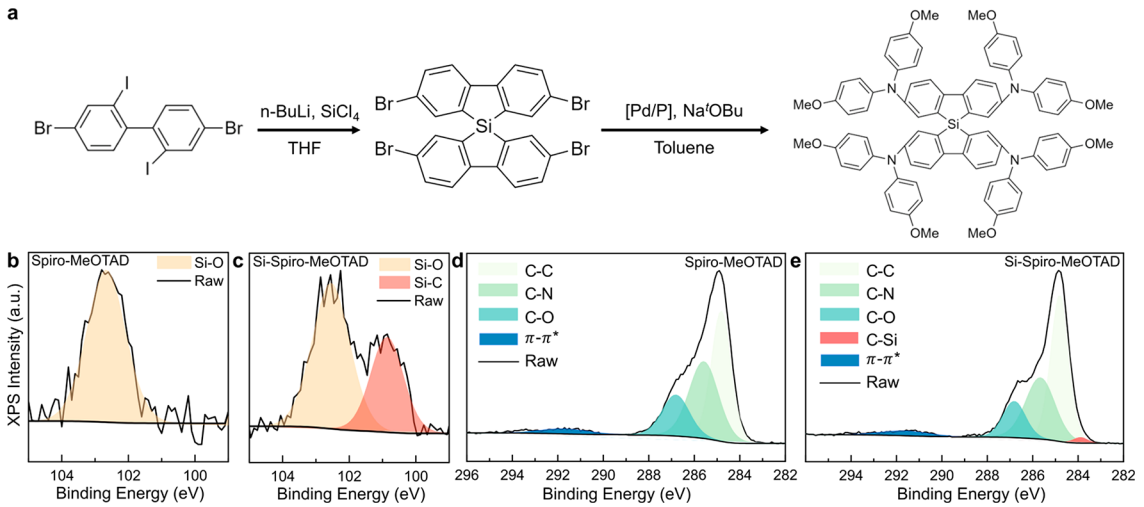

Figure 1. Chemical signatures of Spiro-MeOTADs. (a) Synthesis process of Si-substituted Spiro-MeOTAD (Si-Spiro-MeOTAD). X-ray photoelectron spectroscopy (XPS) spectra of the Si 2p region for (b) Spiro-MeOTAD and (c) Si-Spiro-MeOTAD. Peak fitting of XPS spectra of the C 1s region for (d) Spiro-MeOTAD and (e) Si-Spiro-MeOTAD films.

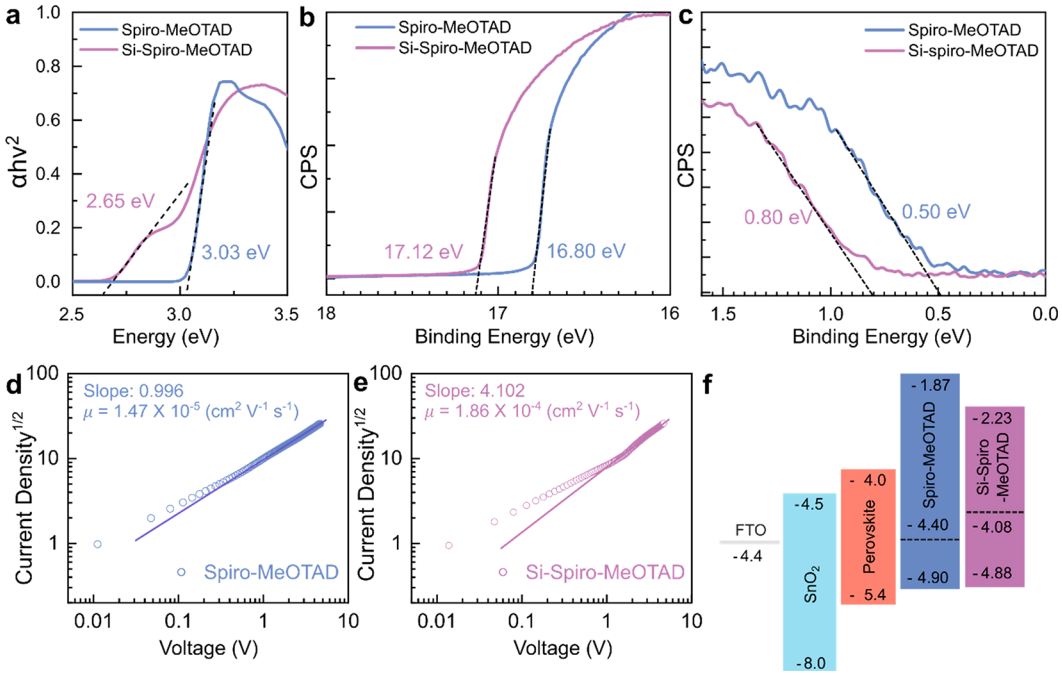

Figure 2. Optoelectronic property of Spiro-MeOTADs. (a) Tauc plot from the UV−vis absorption spectra of Si-Spiro-MeOTAD and Spiro-MeOTAD films. (b) Secondary electron cutoff and (c) valence band of UPS spectra for Spiro-MeOTAD and Si-Spiro-MeOTAD films. Space-charge-limited currents of hole only devices with (d) Spiro-MeOTAD and (e) Si-Spiro-MeOTAD. (f) Schematic illustration of energy levels for perovskite solar cell devices with Spiro-MeOTAD and Si-Spiro-MeOTAD.

spirobifluorene-based derivatives have focused on their functional groups, and some of these attempts have been successful with PSCs.[22] However, these derivatives have not been widely adopted in devices, likely due to their inconsistency in performance. Alternatively, varying the center atom may dramatically alter the optoelectronic and material properties of the HTM. Si, an atom larger than the C atom, could change the packing property of HTMs that are on top of vulnerable perovskite layers, thus influencing the charge extraction and ion migration or air/moisture penetration that affects long-term stability.

In this study, we present the substitution of the central carbon of Spiro-MeOTAD with Si and explore its impacts on the material and solar cell devices. We demonstrate that the substitution of the center carbon atom with a Si atom enhances the perovskite device performance and operational stability. The photovoltaic performance enhancement that is achieved by using the Si-substituted Spiro-MeOTAD (termed Si-Spiro or Si-Spiro-MeOTAD) is substantiated by increasing the hole mobility. This enhanced hole mobility can be explained by an increase in the $\pi-\pi$ stacking ratio and the lower hole reorganization energy estimated from density function theory (DFT) for Si-Spiro. Electron beam-induced current (EBIC) measurements experimentally demonstrate that using Si-Spiro yields a better HTM/perovskite interface, resulting in an improved hole collection in devices. By employing Si-Spiro as

https://doi.org/10.1021/acsenergylett.3c01964
ACS Energy Lett. 2023, 8, 5003−5011

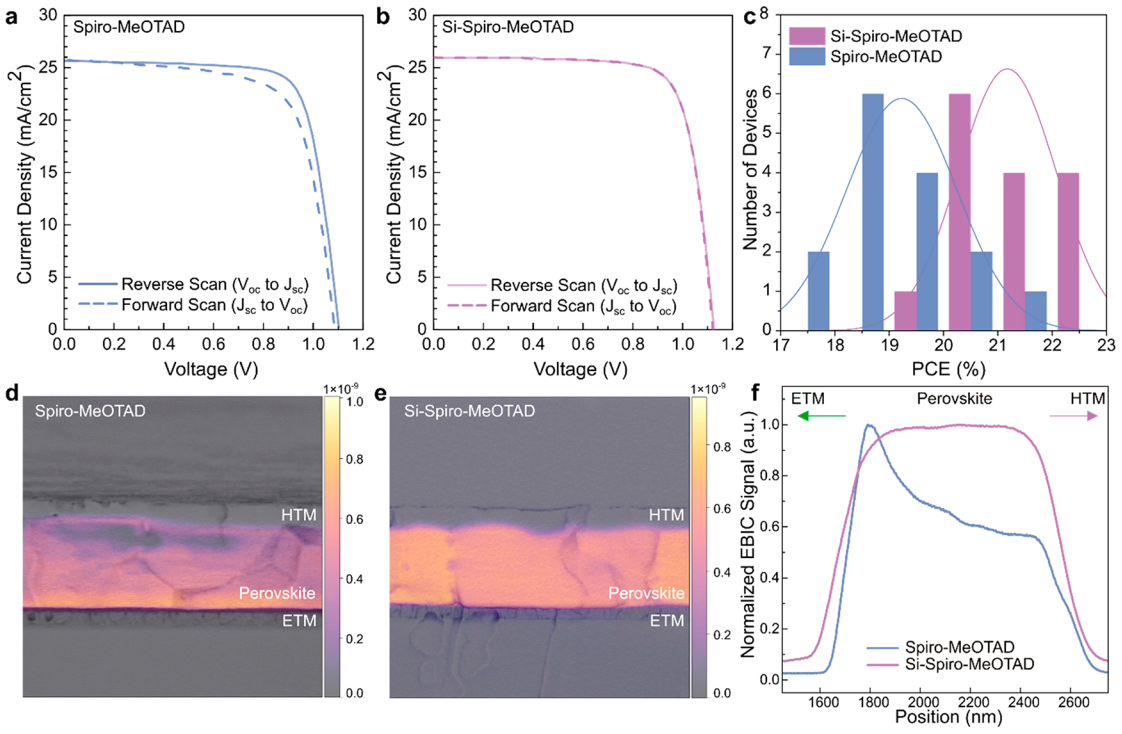

Figure 3. Enhanced carrier collection with Si-Spiro-MeOTAD. Current−voltage curves of reverse scan (from V_{oc} to J_{sc}) and forward scan (from J_{sc} to V_{oc}) of PSCs with (a) Spiro-MeOTAD as the HTM and (b) Si-Spiro-MeOTAD as the HTM. (c) Statistical histogram of PSCs with Spiro-MeOTAD and Si-Spiro-MeOTAD as HTMs. Electron beam-induced current mapping on SEM images for PSCs with (d) Spiro-MeOTAD and (e) Si-Spiro-MeOTAD HTMs. (f) Representative EBIC line profiles for PSCs with Spiro-MeOTAD and Si-Spiro-MeOTAD as HTMs.

the HTM, we achieved a remarkable PCE of 22.5% without any hysteresis, surpassing the PCE that was obtained when using Spiro-MeOTAD. The Si-Spiro-based PSCs achieved superior long-term stability, maintaining over 90% of their performance over 120 h, while the Spiro-based PSCs degrade below 90% within only 20 h. Depth-profiling X-ray photoelectron spectroscopy (XPS) showed the effective blocking Si-Spiro HTMs have against metal ion migration due to strong intermolecular interactions, as was also indicated by the cohesive energy obtained from DFT calculations.

The chemical and optoelectronic properties of Spiro-MeOTAD are altered significantly upon the substitution of the center atom to form Si-Spiro. Figure 1a illustrates the chemical synthesis process of Si-Spiro, and the specific pathway is elaborated in the Materials and Methods section. The ^{1}H NMR spectrum of Si-Spiro is presented in Figure S1. To investigate the chemical changes, X-ray photoelectron spectroscopy (XPS) was employed. The full spectra of the XPS measurement are provided in Figure S2. The XPS spectra of Si 2p for both HTMs, as depicted in Figure 1b,c, reveal the presence of Si−C bonding exclusively in Si-Spiro, whereas the substrate Si−O peak appears in both spectra. The XPS spectra of C 1s for both HTMs (Figure 1d,e) display C−C (∼284.8 eV), C−N (∼285.6 eV), C−O (∼286.8 eV), and $\pi-\pi^*$ satellite (∼291.7 eV) in varying ratios, which are summarized in Table S1. In the XPS spectra of Si-Spiro, a small contribution from C−Si (∼283.9 eV) was detected, which again confirms the result of the Si substitution. The significant increase in the residue of raw data compared to the fitted line after excluding the C−Si bond confirms the existence of the C−Si bond in Si-Spiro (Figure S3). The peak positions in the XPS spectra measured from both HTMs were in good agreement with previous studies.[23,24] The $\pi-\pi$ stacking behavior of the HTM composites plays a crucial role in the hole mobility, as hole carrier transportation occurs via hopping through the $\pi-\pi$ stacked intermolecular interactions.[25,26] The $\pi-\pi^*$ ratio in the XPS data is indicative of the total π-conjugation in the system.[27,28] The substitution of Si does not induce any alterations in the π-bonding configurations within the chemical structures of both Si-Spiro and Spiro-MeOTAD. Consequently, any variations observed in the $\pi-\pi^*$ peaks can be primarily attributed to $\pi-\pi$ stacking interactions. Considering the chemical structure of Spiro-MeOTAD and Si-Spiro, the ratio of the C−N bond can be assumed to be consistent, which can be confirmed by the similar peak position and shape of the N 1s spectra for both HTMs (Figure S4). Therefore, to quantitatively analyze the amount of $\pi-\pi^*$, we calculated the ratio of the $\pi-\pi^*$ peak to the C−N peak. Notably, Si-Spiro (13.96%) has a higher $\pi-\pi^*$ ratio than Spiro-MeOTAD (11.68%); this indicates greater $\pi-\pi$ stacking behavior, which should facilitate efficient hole carrier hopping transportation that can enhance the performance of PSCs.

To further explore the optoelectronic properties of Si-Spiro, Figure 2a presents the Tauc plot derived from the ultraviolet−visible (UV−vis) spectra. For these measurements, Spiro-MeOTAD and Si-Spiro thin films were deposited on indium tin oxide (ITO)/glass substrates. A comprehensive summary of the optoelectronic properties for both the Spiro-MeOTAD and Si-Spiro devices can be found in Table S2. The Tauc plot reveals the optical bandgap of each film, indicating that Si-Spiro has a slightly smaller bandgap. The bandgap of small molecular organic semiconductors tends to decrease as the size of the molecule or the conjugated system increases, as larger molecules have more closely spaced energy levels, which

https://doi.org/10.1021/acsenergylett.3c01964
ACS Energy Lett. 2023, 8, 5003−5011

results in a small energy difference between the highest occupied molecular orbital (HOMO) and the lowest unoccupied molecular orbital (LUMO).[29] However, the HOMO−LUMO gap of organic materials is more complex than that of inorganic semiconductors due to their molecular conformation and packing structure.[30] The optical red-shift can be further discussed in conjunction with the molecular structure.

Ultraviolet photoelectron spectroscopy (UPS) was used to further elucidate the energetic changes; the secondary electron cutoff is plotted in Figure 2b and the valence band region is plotted in Figure 2c. The UPS spectra indicate that Si-Spiro (−4.88 eV) has a slightly higher HOMO level than Spiro-MeOTAD (−4.90 eV). Typically, there is no significant issue if the HOMO level of the HTM is greater than the valence band maximum level of the perovskite (−5.40 eV), as it does not generate any hole extraction barrier. However, an elevated HOMO level could potentially lead to a decrease in the PSC performance due to thermionic losses for the collected holes.[31] Nevertheless, given the negligible difference between the HOMO levels of the two HTMs, it can be reasonably inferred that the charge collection loss would not exhibit substantial variation. An additional cyclic voltammetry (CV) analysis was conducted to validate the HOMO levels, as shown in Figure S5. In regard to the HOMO levels of the two HTMs, those estimated by the CV measurements have the same shift trend as the UPS results. Combining the Tauc plot analysis with the UPS results, the LUMO level of Spiro-MeOTAD (−1.87 eV) is estimated to be higher than that of Si-Spiro (−2.23 eV), which means it could exhibit a better electron blocking efficiency. However, both LUMO levels are significantly higher than the perovskite conduction band minimum level (−4.0 eV), so they both effectively block undesired electron leakage from the perovskite layers. Energetically, the two HTMs would be expected to have similar hole extraction efficiencies.

Next, the hole mobility was evaluated to understand how effectively the HTM transports hole carriers to the anode. The hole mobility was evaluated by measuring the space-charge-limited current (SCLC) using the ITO/HTM/Au device structure shown in Figure S6. The estimated hole mobility of Si-Spiro, which was calculated using the Mott−Gurney law, is almost 10× higher than that of Spiro-MeOTAD (1.47×10^{-5} cm^2 V^{-1} s^{-1} for Spiro-MeOTAD and 1.86×10^{-4} cm^2 V^{-1} s^{-1} for Si-Spiro). This higher mobility could originate from the charge hopping mechanism through the increased $\pi-\pi$ stacking, which is further substantiated by the reorganization energy calculated by DFT later on. In addition, it was anticipated that an increase in the mobility of the HTM could reduce the charge accumulation at the interface, thus enabling a more efficient charge extraction regardless of the energy band level.[32] Consequently, the higher mobility of Si-Spiro is expected to enhance the photovoltaic performance compared to Spiro-MeOTAD.

These optoelectronic properties that were observed and discussed above suggest that Si-Spiro could potentially outperform Spiro-MeOTAD when used in PSC devices. To validate this hypothesis, we applied both Si-Spiro and Spiro-MeOTAD to a SnO_2 ETM and formamidinium lead iodide ($FAPbI_3$) perovskite absorber-based PSC and evaluated their performances. The results, as presented in panels a and b of Figure 3, clearly demonstrate the superior photovoltaic parameters of Si-Spiro. These graphs show the forward (short-circuit current density (J_{sc}) to open-circuit voltage (V_{oc})) and reverse scans (V_{oc} to J_{sc}) of the current density−voltage ($J-V$) curves for PSCs with Spiro-MeOTAD and Si-Spiro HTMs, respectively. Detailed photovoltaic parameters are listed in Table S3. The champion device with Spiro-MeOTAD achieved a PCE of 21.6% for the reverse scan with the following photovoltaic parameters: a J_{sc} of 25.6 mA/cm^2, a V_{oc} of 1.11 V, and a fill factor (FF) of 76.0%. In contrast, the Si-Spiro-based device achieved a higher PCE of 22.5% with a J_{sc} of 25.9 mA/cm^2, a V_{oc} of 1.12 V, and a FF of 77.1%. To further validate the disparity of the PSC performance depending on HTMs, we fabricated a set of 30 devices with identical ETM and perovskite absorbing layers but with varying HTMs. The statistical histogram, summarized in Figure 3c, indicates that PSCs with Si-Spiro not only perform better but also exhibit a more uniform distribution.

This performance enhancement is mainly attributed to the FF increase (Figure S7), which can be the portion of increased hole transportation from enhanced mobility. Forward scanned $J-V$ curves exhibit a much more significant difference due to the hysteresis behavior. PSCs with an n-i-p structure commonly exhibit severe hysteresis behavior depending on the scanning direction.[33] The significant difference that is observed under the same $J-V$ scan condition is that the hysteresis behavior of the champion device with Si-Spiro has decreased substantially compared to the device based on Spiro-MeOTAD. The hysteresis issue in PSCs is primarily attributed to slow charge transport or extraction, which results in capacitive current characteristics.[34] Therefore, it can be inferred that the significant reduction in hysteresis observed in the device based on the Si-Spiro HTM is due to its improved hole transport, substantiation by SCLC measurement, and/or extraction.

To investigate the difference in charge extraction between the perovskite layer and the HTM for a better understanding of the performance enhancement, we utilized the EBIC method, which enables the direct spatial mapping of carriers and local measurements of charge extraction with the full device structure without additional modification. Typically, photoluminescence (PL) analysis can be performed to compare the charge transfer efficiency at the interface. However, this approach is usually limited to evaluating half devices using individual transporting layers. In contrast, EBIC analysis can provide a more comprehensive evaluation of the interface charge transfer in full devices.[35,36]

Panels d and e of Figure 3 present combined images of cross-sectional EBIC mapping and SEM images of PSCs that were created with Spiro-MeOTAD and Si-Spiro HTMs, respectively. It can be seen that the Si-Spiro device shows overall higher EBIC currents (brighter colors) compared to the Spiro-MeOTAD device, which indicates an improved charge collection efficiency.[37] This is evidenced by comparing the average intensity extracted from the EBIC maps for the Spiro-MeOTAD and Si-Spiro devices, as shown in Figure 3f. This average intensity was extracted from the EBIC mapping data of 18 different regions of PSCs using Spiro-MeOTAD and Si-Spiro, with each set of mapping data provided in Figures S8 and S9, respectively. In the case of the Si-Spiro device, the EBIC current is higher; however, in addition to this, the EBIC line profile is uniform across the device junction. In contrast, the devices fabricated with a Spiro-MeOTAD HTM exhibit a gradual decrease in the current of the EBIC signal as it approaches the HTM interface. This decay suggests a poor HTM/perovskite interface with a high surface recombination

https://doi.org/10.1021/acsenergylett.3c01964
ACS Energy Lett. 2023, 8, 5003−5011

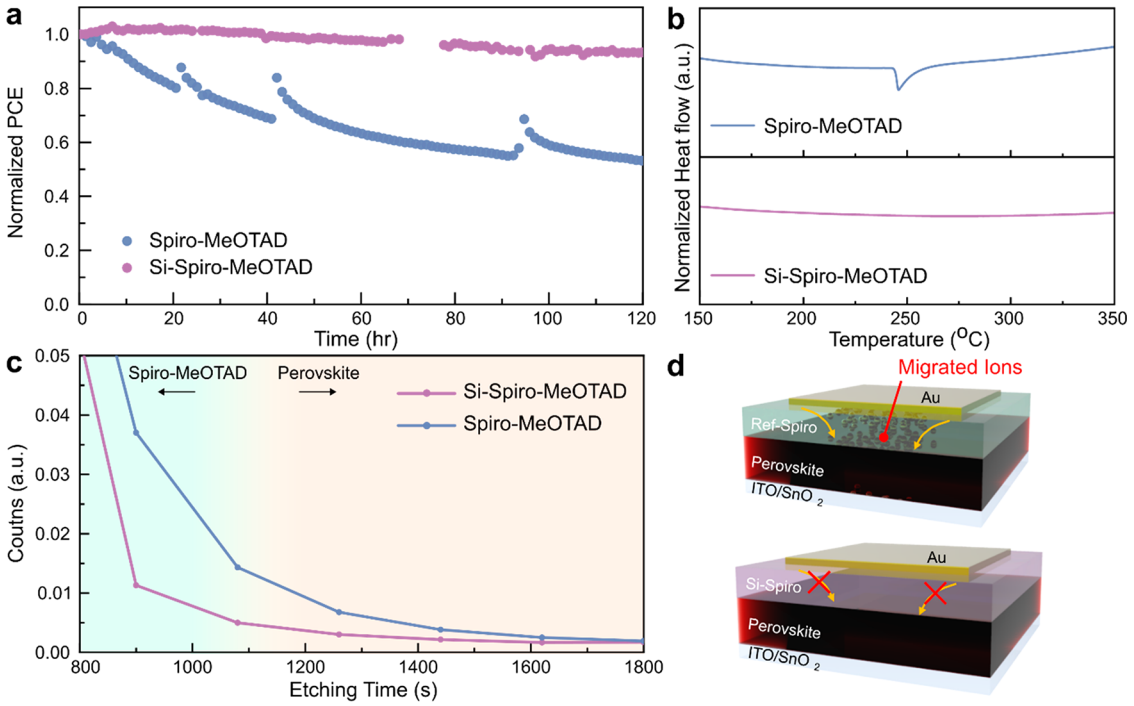

Figure 4. Stability enhancement with Si-Spiro-MeOTAD. (a) Long-term stability evaluation of PSCs with Spiro-MeOTAD and Si-Spiro-MeOTAD as HTMs by tracking the stabilized power output. (b) Thermal characteristics of Spiro-MeOTAD and Si-Spiro-MeOTAD, measured by differential scanning calorimetry. (c) Depth-profiling X-ray photoemission spectral counts of Au atoms through the Spiro-MeOTAD and perovskite layers. (d) Schematics of Au ion migration penetrating perovskite layers.

velocity of selective carriers. This EBIC profile provides evidence for the imbalance between electrons and holes, leading to the observed hysteresis characteristics. Thus, the improved HTM/perovskite interface and high hole mobility of Si-Spiro result in an increased charge collection when incorporated into the device, providing mechanistic evidence of the improved efficiency and V_{oc} in the PSCs, even though the HOMO level of Si-Spiro is slightly higher than that of Spiro-MeOTAD.

The silicon atom in Si-Spiro has a larger atomic radius than the carbon atom in Spiro-MeOTAD, which is expected to cause overall structural changes and changes in its arrangement in the deposited layers. It is anticipated that these changes could lead to alterations in stability. A comparison of the long-term stability of PSCs with different HTMs can be evaluated by tracking the stabilized power output (SPO), as shown in Figure 4a. SPO tracking was conducted with the unencapsulated devices under 1 sun in an Ar atmosphere for 120 h at ambient temperature and 0.77 V. Every recorded raw data point for the SPO tracking is displayed in Figure S10. The PCE of the PSC with Si-Spiro retained 92.9% of the initial PCE after continuous light illumination for 120 h, while the PCE of the PSC with Spiro-MeOTAD only retained 53.2% of the initial PCE. During SPO tracking, intermediate $J-V$ measurements were performed to track the evolution of other device-related parameters, including J_{sc}, FF, and V_{oc}, with the aim of gaining deeper insights into the degradation mechanisms. The $J-V$ sweeping led to abrupt changes in the output power, as shown in Figure 4a. In contrast to the Si-Spiro device, the Spiro-MeOTAD cells showed a recovery in PCE after the $J-V$ sweeping. Notably, these recovery profiles share a reported time scale of ionic migration.[38] The varying magnitudes of the PCE change after $J-V$ sweeping suggest that Si-Spiro has the potential to mitigate the impact of interface-mediated ion migration in devices.

The degradation of PSCs can be attributed to both intrinsic degradation, such as the destruction of the material itself, and degradation resulting from the layer-stacked interfaces. First, the intrinsic molecular stability of the HTMs was assessed using differential scanning calorimetry (DSC). The DSC analysis revealed that Spiro-MeOTAD exhibited an endothermic peak at approximately 240 °C, similar to previous studies.[22,39] In contrast, Si-Spiro showed no distinct endothermic peak up to 350 °C but rather exhibited a broad heat flow, indicating higher thermal stability. This suggests that Si-Spiro possesses enhanced thermal stability, which could contribute to the improved stability of PSCs.

One notable example of degradation resulting from interactions with the surrounding layers is the infiltration of metal Au, which is deposited as an electrode on top of the HTM.[17,40] To investigate this, both HTMs were deposited on top of perovskite layers, and identical Au electrodes were deposited on the HTMs. Subsequently, the samples were exposed to light and heat under 1 sun of illumination for 24 h, and depth-profiling XPS was performed to compare the extent of Au atom penetration into the perovskite layer (Figure 4c). The boundary between Au and the HTM was determined as the etching time when the Au peak rapidly decreased, while the boundary between the HTM and the perovskite layer was determined based on the appearance of the Pb 4f peak of the perovskite (Figures S11 and S12, respectively). It can be seen in Figure 4c,d that Au atoms penetrated significantly less into the perovskite layer beneath Si-Spiro compared to that beneath Spiro-MeOTAD, indicating that long-term stability is likely to be enhanced according to the degradation mechanism revealed in previous studies. As previously discussed, the enhanced $\pi-\pi$ stacking behavior in Si-Spiro leads to strong intermolecular

https://doi.org/10.1021/acsenergylett.3c01964
ACS Energy Lett. 2023, 8, 5003−5011

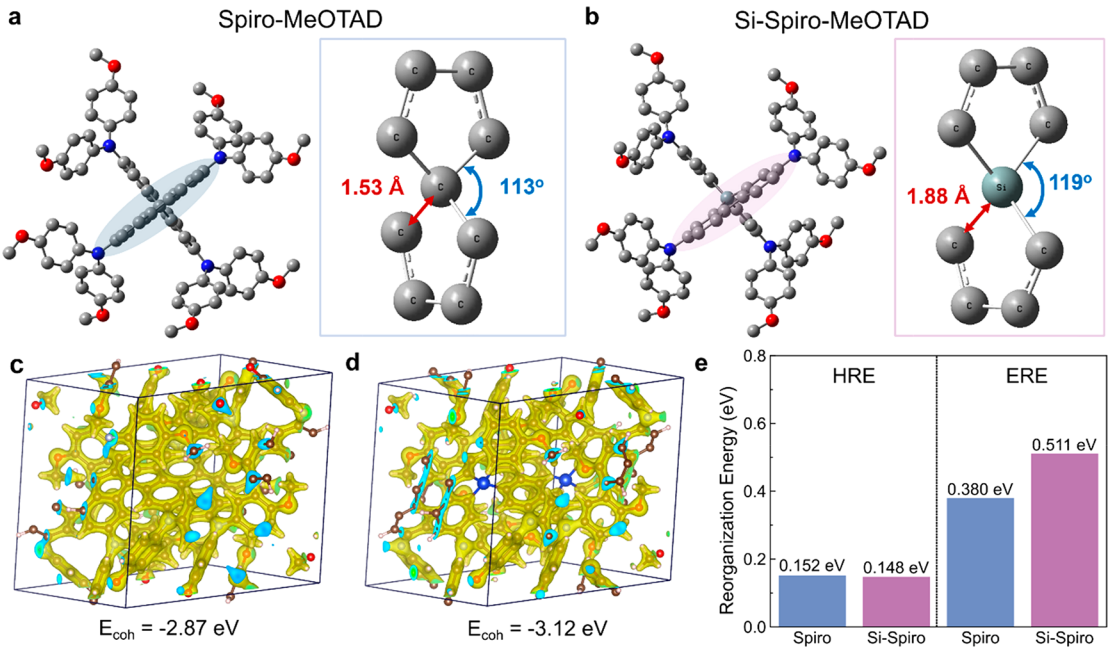

Figure 5. Enhancement evidence of Si-Spiro-MeOTAD via the density functional theory approach. Molecular structure, bond lengths, and angles of (a) Spiro-MeOTAD and (b) Si-Spiro-MeOTAD. Charge density distribution and calculated cohesive energy of (c) Spiro-MeOTAD and (d) Si-Spiro-MeOTAD. (e) Hole reorganization energy (HRE) and electron reorganization energy (ERE) for Spiro-MeOTAD and Si-Spiro-MeOTAD.

interactions, which are the aspect that is attributed to preventing the infiltration of Au atoms through the HTM layer. The forthcoming computational study further supports the presence of such strong intermolecular interactions.

As detailed above, we have confirmed the improvement in performance and stability of PSCs with the use of Si-Spiro as the HTM. Furthermore, we have verified the underlying causes by measuring the intrinsic and extrinsic properties of the materials. Next, to gain a more comprehensive molecular understanding of these effects, we performed density functional theory (DFT) calculations for Spiro-MeOTAD and Si-Spiro. It is interesting to notice from the optimized geometries of the two HTMs that the bond angle of C−Si−C (119°) in Si-Spiro is significantly larger than the corresponding bond angle of C−C−C (113°) in Spiro-MeOTAD (Figure 5a,b). The larger bond angle observed in Si-Spiro provides a more unfolded geometry that leads to it having stronger intermolecular van der Waals interactions with the perovskite layer than Spiro-MeOTAD.[41] For the comparison of such intermolecular interactions among the HTM units, we calculated the thermodynamic energies of the molecular crystal structure to obtain the cohesive energy (E_{coh}) of the molecular crystals via a DFT simulation.[42] It was performed under periodic boundary conditions and was also optimized. The total energies of the unit cell of the HTM and an isolated HTM molecule were also calculated under identical conditions. The cohesive energy of molecular crystals is an important parameter for assessing intermolecular interactions. We calculated the cohesive energy by using the following formula:

$$E_{coh} = \frac{1}{N}E_{bulk} - E_{gas} \quad (1)$$

where E_{bulk} is the total energy of the unit cell, E_{gas} is the energy of an isolated molecule, and N is the number of molecules per unit cell. The calculated cohesive energy of Spiro-MeOTAD was −2.87 eV. In the case of Si-Spiro, we modeled the crystal structure by replacing the central spiro carbon atom with a silicon atom and fully relaxed the system, including the lattice parameters. The calculated cohesive energy of Si-Spiro was −3.12 eV. The more negative cohesive energy (by 0.25 eV) of Si-Spiro is expected to induce stronger intermolecular van der Waals interactions. Furthermore, we investigated the difference in cohesive energy by plotting the total charge density isosurfaces. As shown in Figure 5c,d, the charge density is evenly distributed over the spiro core and methoxyphenyl groups in Spiro-MeOTAD.[43] On the contrary, in the case of Si-Spiro, the charge density is shifted to methoxyphenyl groups from the spiro core. The concentrated charge density on the methoxyphenyl groups in Si-Spiro leads to strong intermolecular interactions. Because of the increased interactions in Si-Spiro, its unit cell volume (2984.75 Å^3) is decreased compared to that of Spiro-MeOTAD (3193.55 Å^3). The improved cohesive energy and strong intermolecular interactions in Si-Spiro can render excellent stability to Si-Spiro-based PSCs. Because of the stronger intermolecular interactions in Si-Spiro, tighter molecular packing and a denser HTM are formed on the perovskite. As a result, it can be assumed that the degradation caused by the penetration of the Au metal can be effectively blocked, as shown in Figure 4c.

To validate the improved hole mobility of Si-Spiro, we compared the carrier mobilities of Si-Spiro and Spiro-MeOTAD by calculating the reorganization energy via a DFT simulation.[44,45] As per the Marcus theory, for high charge hopping and a high charge carrier mobility, the corresponding reorganization energy (λ_h for hole reorganization energy and λ_e for electron reorganization energy) must have a lower value.[46] The computed λ_h and λ_e values are shown in Figure 5e. For the two selected HTMs, the λ_h values are significantly lower than their corresponding λ_e values, which is as expected, as both HTMs are more suitable for hole transportation than for

https://doi.org/10.1021/acsenergylett.3c01964
ACS Energy Lett. 2023, 8, 5003−5011

electron transportation. The smaller λ_h value (0.148 eV) of Si-Spiro compared to that of Spiro-MeOTAD (0.152 eV) may enhance its hole mobility and the performance of Si-Spiro in a PSC over Spiro-MeOTAD. Furthermore, we calculated the electron−hole exciton binding energy to validate the better photovoltaic performance of Si-Spiro-based PSCs. We calculated the exciton binding energy by subtracting the optical bandgap (S_1 excitation energy) from the electronic bandgap ($E_{LUMO} - E_{HOMO}$). The calculated exciton binding energies of Spiro-MeOTAD and Si-Spiro were 0.513 and 0.507 eV, respectively, as summarized in Table S4. The lower exciton binding energy of Si-Spiro facilitates an easy charge separation and enhances its hole mobility over that of Spiro-MeOTAD. The calculated exciton binding energy of Spiro-MeOTAD (0.513 eV) is in very good agreement with the previously calculated value (0.510 eV).[46] Moreover, the calculated energy levels and absorption spectra have the same trends as the experimental results (Figures S13 and S14, respectively). Thereby, our simulation results show qualitative and quantitative agreement with the experimental findings that Si-Spiro-based PSCs exhibit enhanced performance and stability.

In this study, we synthesized Si-Spiro-MeOTAD (Si-Spiro) and compared its properties and performance with those of Spiro-MeOTAD in perovskite solar cells (PSCs). The introduction of a silicon atom in place of the central carbon atom in Spiro-MeOTAD resulted in variations in the chemical and optoelectronic properties of the material. X-ray photoelectron spectroscopy (XPS) confirmed an increased portion of the $\pi-\pi$ stacking interaction; this resulted in an enhanced hole mobility by carrier hopping, which was further evidenced by space-charge-limited current (SCLC) measurements. This higher hole mobility and altered molecular structure of Si-Spiro contributed to the enhanced performance and stability in PSCs. The devices that used Si-Spiro as a hole transport material (HTM) demonstrated superior photovoltaic parameters and a more uniform distribution of performance as well as improved long-term stability. Cross-sectional electron beam-induced current (EBIC) mapping further confirmed the improved charge collection efficiency in Si-Spiro-based devices, and depth-profiling XPS showed that metal ion migration through Si-Spiro is significantly decreased compared to that through Spiro-MeOTAD. Theoretical calculations using density functional theory (DFT) supported these experimental findings, revealing a larger bond angle in Si-Spiro that leads to stronger intermolecular van der Waals interactions and an improved cohesive energy. The results of this study highlight the potential of Si-Spiro as a promising HTM for use in PSCs, offering opportunities for the development of solar cells with enhanced performance and stability.

■ ASSOCIATED CONTENT

Supporting Information

The Supporting Information is available free of charge at https://pubs.acs.org/doi/10.1021/acsenergylett.3c01964.

Materials and Methods section; full XPS spectra; SEM images; CV curves; DFT-calculated optical properties; NMR spectrum of HTMs; statistical box plots of J_{sc}, V_{oc}, and FF; combined EBIC scans and SEM images; depth-profiling XPS data for devices with HTMs; atomic proportion from XPS spectra; optoelectronic properties; summarized photovoltaic parameters; and calculated exciton binding energies (PDF)

■ AUTHOR INFORMATION

Corresponding Authors

Joonkyung Jang − *Department of Nanoenergy Engineering, Pusan National University, Busan, Republic of Korea 46241;* orcid.org/0000-0001-9028-0605; Email: jkjang@pusan.ac.kr

David P. Fenning − *Materials Science and Engineering Program, University of California San Diego, La Jolla, California 92093, United States; Department of NanoEngineering, University of California San Diego, La Jolla, California 92093, United States;* orcid.org/0000-0002-4609-9312; Email: dfenning@eng.ucsd.edu

Min-cheol Kim − *School of Mechanical Engineering, Pusan National University, Busan 46241, Korea;* orcid.org/0000-0001-8292-8117; Email: mckim90@pusan.ac.kr

Authors

Yanqi Luo − *Advanced Photon Source, Argonne National Laboratory, Lemont, Illinois 60439, United States*

Ramesh Kumar Chitumalla − *Department of Nanoenergy Engineering, Pusan National University, Busan, Republic of Korea 46241;* orcid.org/0000-0002-9523-7056

So-Yeon Ham − *Materials Science and Engineering Program, University of California San Diego, La Jolla, California 92093, United States*

Deniz N. Cakan − *Department of NanoEngineering, University of California San Diego, La Jolla, California 92093, United States;* orcid.org/0000-0001-5177-8654

Taewoo Kim − *Materials Science Division, Argonne National Laboratory, Lemont, Illinois 60439, United States*

Sanghyun Paek − *Department of Chemistry and Energy Engineering, Sangmyung University, Seoul 03016, Republic of Korea*

Ying Shirley Meng − *Department of NanoEngineering, University of California San Diego, La Jolla, California 92093, United States; Pritzker School of Molecular Engineering, University of Chicago, Chicago, Illinois 60637, United States;* orcid.org/0000-0001-8936-8845

Complete contact information is available at: https://pubs.acs.org/10.1021/acsenergylett.3c01964

Author Contributions

[⊥]Y.L. and R.K.C. contributed equally to this work. Y.L., Y.S.M., D.P.F., and M.-c.K. conceived the idea and designed the project. J.J., D.P.F., and M.-c.K. supervised the project. S.P. synthesized the materials, and Y.L., S.-Y.H., and M.-c.K. fabricated the PSC devices. Y.L. and T.K. performed the material characterization, and S.-Y.H. and D.N.C. performed the EBIC analysis. Y.S.M., D.P.F., and M.-c.K. analyzed the material characterization results. R.K.C. and J.J. performed the DFT simulations. Y.L. and M.-c.K. wrote the original draft, and all co-authors reviewed and edited the manuscript.

Notes

The authors declare no competing financial interest.

■ ACKNOWLEDGMENTS

This work was supported by a National Research Foundation of Korea (NRF) grant funded by the Korean government (MSIT) (2022R1C1C1003403) for M.-C.K. The UC San

Diego portion of the work was supported in part by the California Energy Commission (EPC-16-050 and EPC-19-004). Si-Spiro-MeOTAD was provided by MilliporeSigma (Catalog No. 924164). J.J. acknowledges the support by the National Research Foundation of Korea (NRF) grant funded by the Korea government (MSIT) (RS-2023-00220748).

REFERENCES

(1) Kojima, A.; Teshima, K.; Shirai, Y.; Miyasaka, T. Organometal halide perovskites as visible-light sensitizers for photovoltaic cells. *Journal of the American chemical society* **2009**, *131* (17), 6050−6051.
(2) Lee, G.; Kim, M.-c.; Choi, Y. W.; Ahn, N.; Jang, J.; Yoon, J.; Kim, S. M.; Lee, J.-G.; Kang, D.; Jung, H. S.; Choi, M. Ultra-flexible perovskite solar cells with crumpling durability: Toward a wearable power source. *Energy Environ. Sci.* **2019**, *12* (10), 3182−3191.
(3) Li, Z.; Klein, T. R.; Kim, D. H.; Yang, M.; Berry, J. J.; van Hest, M. F.; Zhu, K. Scalable fabrication of perovskite solar cells. *Nat. Rev. Mater.* **2018**, *3* (4), 18017.
(4) Burschka, J.; Pellet, N.; Moon, S.-J.; Humphry-Baker, R.; Gao, P.; Nazeeruddin, M. K.; Grätzel, M. Sequential deposition as a route to high-performance perovskite-sensitized solar cells. *Nature* **2013**, *499* (7458), 316−319.
(5) Jeon, N. J.; Noh, J. H.; Kim, Y. C.; Yang, W. S.; Ryu, S.; Seok, S. I. Solvent engineering for high-performance inorganic-organic hybrid perovskite solar cells. *Nature materials* **2014**, *13* (9), 897−903.
(6) Kim, H.-S.; Lee, C.-R.; Im, J.-H.; Lee, K.-B.; Moehl, T.; Marchioro, A.; Moon, S.-J.; Humphry-Baker, R.; Yum, J.-H.; Moser, J. E.; Grätzel, M.; Park, N.-G. Lead iodide perovskite sensitized all-solid-state submicron thin film mesoscopic solar cell with efficiency exceeding 9%. *Sci. Rep.* **2012**, *2* (1), 591.
(7) Best Research-Cell Efficiency Chart. National Renewable Energy Laboratory (REL). https://www.nrel.gov/pv/cell-efficiency.html. (accessed 2023-07-17).
(8) K Rao, M.; Sangeetha, D.N.; Selvakumar, M.; Sudhakar, Y.N.; Mahesha, M.G. Review on persistent challenges of perovskite solar cells' stability. *Sol. Energy* **2021**, *218*, 469−491.
(9) Rombach, F. M.; Haque, S. A.; Macdonald, T. J. Lessons learned from spiro-OMeTAD and PTAA in perovskite solar cells. *Energy Environ. Sci.* **2021**, *14* (10), 5161−5190.
(10) Bao, Q.; Liu, X.; Braun, S.; Fahlman, M. Oxygen-and water-based degradation in [6, 6]-phenyl-C61-butyric acid methyl ester (PCBM) films. *Adv. Energy Mater.* **2014**, *4* (6), 1301272.
(11) Kim, M.-c.; Ahn, N.; Cheng, D.; Xu, M.; Ham, S.-Y.; Pan, X.; Kim, S. J.; Luo, Y.; Fenning, D. P.; Tan, D. H. S.; Zhang, M.; Zhu, G.; Jeong, K.; Choi, M.; Meng, Y. S. Imaging real-time amorphization of hybrid perovskite solar cells under electrical biasing. *ACS Energy Letters* **2021**, *6* (10), 3530−3537.
(12) Jacobs, D. A.; Wolff, C. M.; Chin, X.-Y.; Artuk, K.; Ballif, C.; Jeangros, Q. Lateral ion migration accelerates degradation in halide perovskite devices. *Energy Environ. Sci.* **2022**, *15* (12), 5324−5339.
(13) Yin, X.; Song, Z.; Li, Z.; Tang, W. Toward ideal hole transport materials: a review on recent progress in dopant-free hole transport materials for fabricating efficient and stable perovskite solar cells. *Energy Environ. Sci.* **2020**, *13* (11), 4057−4086.
(14) Rai, N.; Rai, S.; Singh, P. K.; Lohia, P.; Dwivedi, D. Analysis of various ETL materials for an efficient perovskite solar cell by numerical simulation. *Journal of Materials Science: Materials in Electronics* **2020**, *31*, 16269−16280.
(15) Kim, M.-c.; Ahn, N.; Lim, E.; Jin, Y. U.; Pikhitsa, P. V.; Heo, J.; Kim, S. K.; Jung, H. S.; Choi, M. Degradation of CH 3 NH 3 PbI 3 perovskite materials by localized charges and its polarity dependency. *Journal of Materials Chemistry A* **2019**, *7* (19), 12075−12085.
(16) Park, J.; Kim, J.; Yun, H.-S.; Paik, M. J.; Noh, E.; Mun, H. J.; Kim, M. G.; Shin, T. J.; Seok, S. I. Controlled growth of perovskite layers with volatile alkylammonium chlorides. *Nature* **2023**, *616* (7958), 724−730.
(17) Domanski, K.; Correa-Baena, J.-P.; Mine, N.; Nazeeruddin, M. K.; Abate, A.; Saliba, M.; Tress, W.; Hagfeldt, A.; Grätzel, M. Not all that glitters is gold: metal-migration-induced degradation in perovskite solar cells. *ACS Nano* **2016**, *10* (6), 6306−6314.
(18) Kim, J.; Park, N.; Yun, J. S.; Huang, S.; Green, M. A.; Ho-Baillie, A. W. An effective method of predicting perovskite solar cell lifetime-Case study on planar CH3NH3PbI3 and HC (NH2) 2PbI3 perovskite solar cells and hole transfer materials of spiro-OMeTAD and PTAA. *Sol. Energy Mater. Sol. Cells* **2017**, *162*, 41−46.
(19) Wang, S.; Cabreros, A.; Yang, Y.; Hall, A. S.; Valenzuela, S.; Luo, Y.; Correa-Baena, J.-P.; Kim, M.-c.; Fjeldberg, Ø.; Fenning, D. P.; Meng, Y. S. Impacts of the hole transport layer deposition process on buried interfaces in perovskite solar cells. *Cell Reports Physical Science* **2020**, *1* (7), 100103.
(20) Jeon, N. J.; Lee, H. G.; Kim, Y. C.; Seo, J.; Noh, J. H.; Lee, J.; Seok, S. I. o-Methoxy substituents in spiro-OMeTAD for efficient inorganic-organic hybrid perovskite solar cells. *J. Am. Chem. Soc.* **2014**, *136* (22), 7837−7840.
(21) Ren, G.; Han, W.; Deng, Y.; Wu, W.; Li, Z.; Guo, J.; Bao, H.; Liu, C.; Guo, W. Strategies of modifying spiro-OMeTAD materials for perovskite solar cells: a review. *Journal of Materials Chemistry A* **2021**, *9* (8), 4589−4625.
(22) Jeong, M.; Choi, I. W.; Yim, K.; Jeong, S.; Kim, M.; Choi, S. J.; Cho, Y.; An, J.-H.; Kim, H.-B.; Jo, Y.; Kang, S.-H.; Bae, J.-H.; Lee, C.-W.; Kim, D. S.; Yang, C. Large-area perovskite solar cells employing spiro-Naph hole transport material. *Nat. Photonics* **2022**, *16* (2), 119−125.
(23) Hawash, Z.; Ono, L. K.; Qi, Y. Moisture and Oxygen Enhance Conductivity of LiTFSI-Doped Spiro-MeOTAD Hole Transport Layer in Perovskite Solar Cells. *Advanced Materials Interfaces* **2016**, *3* (13), 1600117.
(24) Ono, L. K.; Schulz, P.; Endres, J. J.; Nikiforov, G. O.; Kato, Y.; Kahn, A.; Qi, Y. Air-exposure-induced gas-molecule incorporation into spiro-MeOTAD films. *journal of physical chemistry letters* **2014**, *5* (8), 1374−1379.
(25) Kang, I.; Yun, H.-J.; Chung, D. S.; Kwon, S.-K.; Kim, Y.-H. Record high hole mobility in polymer semiconductors via side-chain engineering. *J. Am. Chem. Soc.* **2013**, *135* (40), 14896−14899.
(26) Tseng, H.-R.; Phan, H.; Luo, C.; Wang, M.; Perez, L. A.; Patel, S. N.; Ying, L.; Kramer, E. J.; Nguyen, T.-Q.; Bazan, G. C.; Heeger, A. J. High-mobility field-effect transistors fabricated with macroscopic aligned semiconducting polymers. *Adv. Mater.* **2014**, *26* (19), 2993−2998.
(27) France, R. M.; Short, R. D. Plasma treatment of polymers: the effects of energy transfer from an argon plasma on the surface chemistry of polystyrene, and polypropylene. A high-energy resolution X-ray photoelectron spectroscopy study. *Langmuir* **1998**, *14* (17), 4827−4835.
(28) Huang, P.; Xiong, T.; Zhou, S.; Yang, H.; Huang, Y.; Balogun, M.-S. J. T.; Ding, Y. Advanced Tri-Layer Carbon Matrices with π-π Stacking Interaction for Binder-Free Lithium-Ion Storage. *ACS Appl. Mater. Interfaces* **2021**, *13* (14), 16516−16527.
(29) Costa, J. C.; Taveira, R. J.; Lima, C. F.; Mendes, A.; Santos, L. M. Optical band gaps of organic semiconductor materials. *Opt. Mater.* **2016**, *58*, 51−60.
(30) Chen, Z.; Li, H.; Tao, Y.; Chen, L.; Chen, C.; Jiang, H.; Xu, S.; Zhou, X.; Chen, R.; Huang, W. Tuning intramolecular conformation and packing mode of host materials through noncovalent interactions for high-efficiency blue electrophosphorescence. *ACS omega* **2019**, *4* (5), 9129−9134.
(31) Schulz, P.; Edri, E.; Kirmayer, S.; Hodes, G.; Cahen, D.; Kahn, A. Interface energetics in organo-metal halide perovskite-based photovoltaic cells. *Energy Environ. Sci.* **2014**, *7* (4), 1377−1381.
(32) Shoaee, S.; Stolterfoht, M.; Neher, D. The Role of Mobility on Charge Generation, Recombination, and Extraction in Polymer-Based Solar Cells. *Adv. Energy Mater.* **2018**, *8* (28), 1703355.
(33) Kang, D.-H.; Park, N.-G. On the current-voltage hysteresis in perovskite solar cells: dependence on perovskite composition and methods to remove hysteresis. *Adv. Mater.* **2019**, *31* (34), 1805214.
(34) Singh, R.; Parashar, M. Chapter 1: Origin of Hysteresis in Perovskite Solar Cells. In *Soft-Matter Thin Film Solar Cells: Physical*

Processes and Device Simulation; Ren, J., Kan, Z., Eds.; AIP Publishing LLC, 2020; p 1-1−1-42. DOI: 10.1063/9780735422414_001.
(35) Wang, R.; Xue, J.; Wang, K.-L.; Wang, Z.-K.; Luo, Y.; Fenning, D.; Xu, G.; Nuryyeva, S.; Huang, T.; Zhao, Y.; Yang, J. L.; Zhu, J.; Wang, M.; Tan, S.; Yavuz, I.; Houk, K. N.; Yang, Y. Constructive molecular configurations for surface-defect passivation of perovskite photovoltaics. *Science* **2019**, *366* (6472), 1509−1513.
(36) Correa-Baena, J.-P.; Luo, Y.; Brenner, T. M.; Snaider, J.; Sun, S.; Li, X.; Jensen, M. A.; Hartono, N. T. P.; Nienhaus, L.; Wieghold, S.; Poindexter, J. R.; Wang, S.; Meng, Y. S.; Wang, T.; Lai, B.; Holt, M. V.; Cai, Z.; Bawendi, M. G.; Huang, L.; Buonassisi, T.; Fenning, D. P. Homogenized halides and alkali cation segregation in alloyed organic-inorganic perovskites. *Science* **2019**, *363* (6427), 627−631.
(37) Edri, E.; Kirmayer, S.; Mukhopadhyay, S.; Gartsman, K.; Hodes, G.; Cahen, D. Elucidating the charge carrier separation and working mechanism of CH3NH3PbI3- x Cl x perovskite solar cells. *Nat. Commun.* **2014**, *5* (1), 3461.
(38) Domanski, K.; Roose, B.; Matsui, T.; Saliba, M.; Turren-Cruz, S.-H.; Correa-Baena, J.-P.; Carmona, C. R.; Richardson, G.; Foster, J. M.; De Angelis, F.; Ball, J. M.; Petrozza, A.; Mine, N.; Nazeeruddin, M. K.; Tress, W.; Gratzel, M.; Steiner, U.; Hagfeldt, A.; Abate, A. Migration of cations induces reversible performance losses over day/night cycling in perovskite solar cells. *Energy Environ. Sci.* **2017**, *10* (2), 604−613.
(39) Malinauskas, T.; Tomkute-Luksiene, D.; Sens, R. d.; Daskeviciene, M.; Send, R.; Wonneberger, H.; Jankauskas, V.; Bruder, I.; Getautis, V. Enhancing thermal stability and lifetime of solid-state dye-sensitized solar cells via molecular engineering of the hole-transporting material spiro-OMeTAD. *ACS Appl. Mater. Interfaces* **2015**, *7* (21), 11107−11116.
(40) Kerner, R. A.; Zhao, L.; Harvey, S. P.; Berry, J. J.; Schwartz, J.; Rand, B. P. Low threshold voltages electrochemically drive gold migration in halide perovskite devices. *ACS Energy Letters* **2020**, *5* (11), 3352−3356.
(41) Grimme, S.; Antony, J.; Ehrlich, S.; Krieg, H. A consistent and accurate ab initio parametrization of density functional dispersion correction (DFT-D) for the 94 elements H-Pu. *J. Chem. Phys.* **2010**, *132* (15), 154104.
(42) Kresse, G.; Hafner, J. Ab initio molecular-dynamics simulation of the liquid-metal-amorphous-semiconductor transition in germanium. *Phys. Rev. B* **1994**, *49* (20), 14251−14269.
(43) Perdew, J. P.; Burke, K.; Ernzerhof, M. Generalized Gradient Approximation Made Simple. *Phys. Rev. Lett.* **1996**, *77* (18), 3865−3868.
(44) Thomas, A.; Chitumalla, R. K.; Puyad, A. L.; Mohan, K. V.; Jang, J. Computational studies of hole/electron transport in positional isomers of linear oligo-thienoacenes: Evaluation of internal reorganization energies using density functional theory. *Computational and Theoretical Chemistry* **2016**, *1089*, 59−67.
(45) Kumar, V.; Tripathi, A.; Choi, S.; Chitumalla, R. K.; Seo, J.-Y.; Jang, J.; Chetti, P. Density functional theory and time-dependent density functional theory studies on optoelectronic properties of fused heterocycles with cyclooctatetraene. *Bulletin of the Korean Chemical Society* **2022**, *43* (7), 990−998.
(46) Alberga, D.; Mangiatordi, G. F.; Labat, F.; Ciofini, I.; Nicolotti, O.; Lattanzi, G.; Adamo, C. Theoretical Investigation of Hole Transporter Materials for Energy Devices. *J. Phys. Chem. C* **2015**, *119* (42), 23890−23898.

https://doi.org/10.1021/acsenergylett.3c01964
ACS Energy Lett. 2023, 8, 5003−5011